Check for updates

SHG-enhanced NIR-excited *in vitro* photodynamic therapy using composite nanoparticles of barium titanate and rose Bengal†

Xianhe Sun,[a] Zhang Ji [ID][a] and Sailing He [ID]*[ab]

Near infrared (NIR) light excited photodynamic therapy (PDT) has been considered as a possible way to increase the therapy depth. Besides the traditional two-photon excited PDT and upconversion PDT by rare-earth ion materials, SHG has drawn much attention recently to act as an additional choice to achieve NIR light excited PDT. Herein, by using the electrostatic absorption method, barium titanate and rose Bengal composite nanoparticles (BT@PAH/RB/PAH, BT–RB) were synthesized. Compared with rose Bengal (RB) molecules and a mixture of barium titanate nanoparticles and RB (BT + RB), BT–RB nanoparticles were shown to be able to produce more reactive oxygen species (ROS) *ex vivo* and *in vitro*. Afterwards, the SHG-enhanced localized PDT was applied on Hela cells, in which BT–RB nanoparticles showed a better performance than BT + RB. Our work has shown that the SHG-enhanced PDT has good prospects and the close combination of harmonic nanoparticles and photosensitizers may facilitate the development of novel reagents for NIR light excited PDT.

1. Introduction

Cancer has become the second leading cause of death in humans worldwide, and ranks only behind cardiovascular disease. The latest global cancer data published in 2018 has predicted that new cancer cases would rise by about 63% in two decades.[1] At the same time, people can live longer today,[2] and increased age is believed to be the greatest risk for developing cancers.[3,4] Old people tend to have poor health, and this raises an urgent need for more gentle cancer treatment modalities. Over the past few decades, photodynamic therapy (PDT) has been developed as a novel cancer treatment method with good selectivity.[5–8] Photosensitizers (PSs) under suitable light irradiation can first be excited to the excitation energy level, and then transit to the triplet energy level. The triplet PSs are likely to interact with oxygen or oxygen-containing groups, which would generate toxic reactive oxygen species (ROS) and cause cell apoptosis or necrosis.[9–12] Since the above process (known as photodynamic effect) can only occur when suitable light and PSs are both present, the treatment region can be carefully selected and side effects would be small.

Clinical applications of photo-activated process always need light in near infrared (NIR) range to guarantee the penetration depth of light in tissues due to the absorption and scattering effect.[13–15] Nevertheless, unfortunately, most commercially available PSs can only be excited by visible light so far.[16,17] Creating PSs that absorb NIR light can be a solution, and efforts have been made to excite PSs linearly using NIR light.[13] However, the energy of photons in NIR range is too low to achieve effective excitation, which limits the production of ROS as well.[18] Therefore, the upconversion of NIR photons can be another way to solve this problem.

Rare-earth ion nanoparticles are famous for the ability to transfer NIR light to visible light using continuous wave (CW) light. However, the energy of emission photons are directly determined by the energy level of certain lanthanide ions, which means only a part of PSs that have good absorption ability at certain wavelength could be used in this method.[19]

Upconversion process can also be achieved using nonlinear optical effects. Two-photon absorption (TPA) is a widely used way, in which two photons are absorbed simultaneously and the molecule can be excited to the same energy level as that excited by photon that has double of the energy (thus have half of the wavelength).[20,21] Moreover, since nonlinear effect requires large peak intensity, TPA can only be effectively achieved within the focus spot, which makes it a more precise process.[22] There are efforts to achieve TPA or higher-order excitation of commercialized PSs directly, but the efficiency is rather low.[23,24] To solve the problem, many efforts have been made to modify PSs with certain functional groups to increase the TPA cross section or directly combine PSs with other materials that have high TPA cross section.[25–29] However, the modification procedure can be rather complicated, and the combination needs specific match

[a] *State Key Laboratory of Modern Optical Instrumentations, Centre for Optical and Electromagnetic Research, Zhejiang University, Hangzhou 310058, China*

[b] *Department of Electromagnetic Engineering, School of Electrical Engineering, Royal Institute of Technology, SE-100 44 Stockholm, Sweden. E-mail: sailing@kth.se*

† Electronic supplementary information (ESI) available. See DOI: 10.1039/c9ra00432g

between the absorption spectrum of PS and the fluorescence spectrum of TPA materials, which limits the application of the method.

Compare with TPA effect, second harmonic generation (SHG) is a non-parametric process, in which two photons can be converted to one photon with double of energy (thus half of the wavelength) directly when passing through certain materials without being absorbed.[30] In this process, the wavelength of the generated light can be easily tuned in a wide range by changing the excitation source. Due to the nature of nonlinear effect, SHG effect can also achieve localized excitation. Furthermore, since there is no absorption process, neither transition process nor energy loss is involved in SHG, which means that photobleaching can be totally avoided.[31] In the past few years, SHG has been utilized to achieve NIR excited PDT in different forms. Kachynski, *et al.* have realized *in situ* photodynamic therapy using SHG generated in collagen together with other nonlinear optical effects, but their method might be limited to certain tissue types and structures.[32] Recently, harmonic nanoparticles have also been introduced to SHG-involved PDT. Gu, *et al.* have utilized ZnO nanoparticles to efficiently generate SHG light *in situ* to achieve PDT of chlorin e6 (Ce6, a commonly used photosensitizer) through one-photon excitation.[33] Unfortunately, they did not combine PSs and ZnO as composite nanoparticles. Otherwise, a combination way would enable photon donor and accepter to get closer, which can lead to better results. Very recently, PSs capsulated within coordinate nanoparticles have been used as composite nanoparticles to achieve SHG-mediated PDT on cancer cells.[34] The work focuses on the total PDT effect, but did not study the behaviour and contribution of the components.

Among the commonly used harmonic nanoparticles, barium titanate (BT) nanoparticles have been playing a promising role for SHG-mediated biological applications in recent years.[35] In a systematical survey of five different kinds of harmonic nanoparticles, BT nanoparticles show large normalized hyperpolarizability as well as best biocompatibility.[36] In a study of SHG-mediated *in vivo* imaging, the BT nanoparticles are confirmed to have boarder optimal wavelength range than ZnO and SiC, and the following *in vivo* experiments compared with quantum dots further verified the non-bleaching, non-blinking and non-toxic properties of BT nanoparticles.[37] In 2016, we have also reported barium titanate and Ce6 composite nanoparticles for SHG image-guided one-photon excited photodynamic therapy.[38] Among the commercialized photosensitizers, Rose Bengal (RB) is a common used one with high singlet oxygen quantum yield of 0.75.[39] Moreover, the rose Bengal has strong absorption band around 550 nm, which means the SHG excitation can be achieved using light in the longer-wavelength NIR region (around 1100 nm) than previous works. In the present paper, by combining BT nanoparticles with RB, we shift the excitation source to 1040 nm, and systematically study the improvement of SHG-mediated NIR light excited fluorescence and photodynamic effect and finally achieve the *in vitro* localized and SHG enhanced PDT. Our work indicates that the combination of PSs and harmonic nanoparticles can further improve the efficacy of SHG-mediated NIR light excited PDT,

and shows good potential in developing localized NIR-excited PDT strategies.

2. Experimental

2.1 Materials

Barium titanate nanoparticles, rose Bengal, poly(allylamine hydrochloride) (PAH, MW: 15 000), 9,10-anthracenediyl-bis(methylene)dimalonic acid (ABDA), 1,3-diphenylisobenzofuran (DPBF), 2′,7′-dichlorodihydrofluorescein diacetate (DCFH-DA) and Cell Counting Kit-8 (CCK-8) assay were purchased from Sigma-Aldrich (Shanghai, China), Dulbecco's Modified Eagle's medium (DMEM) and fetal bovine serum (FBS) were bought from Gibco. Annexin V and propidium iodide (PI) were purchased from BioLegend. Phosphate buffer saline (PBS), dimethyl sulfoxide and deionized water were obtained from the Chemical Reagent Department of Zhejiang University.

2.2 Characterization

Absorption spectra were measured by a Shimadzu 2550 UV-vis scanning spectrophotometer; zeta potentials were obtained using Malvern Zetasizer Nano ZS-90; transmission electron microscopic (TEM) images were obtained using a JEOL JEM-1200 transmission electron microscope (operating at 80 kV in bright-field mode); fluorescence spectrum of RB was measured using an F-2500 HITCH fluorescence spectrophotometer; Raman spectra were obtained using a fiber-based Raman probe (BWTEK) under the excitation of 785 nm laser (300 mW).

2.3 SHG detection under fs laser irradiation

The SHG property of BT nanoparticles was verified by using a home-built cage system and 1040 nm fs laser, as illustrated in Fig. S1.† Briefly, the excitation light (1040 nm fs) was guided into an objective lens after passing a 980 nm long-pass filter, then the powder of BT nanoparticles was put on a glass slide placed just at the focus point and the same objective lens was adjusted to collect the signal. After passing a 950 nm short pass filter, the signal was guided into a fiber and finally analyzed by a PG 2000 (Ideaoptics Inc.) spectrometer.

2.4 Fabrication of barium titanate and rose Bengal composite (BT–RB) nanoparticles

The BT–RB nanoparticles were synthesized using the electrostatic absorption method. First, 7.5 mg BT nanoparticles powder was dissolved in 27 ml DI water, followed by 1 h of sonication. When the solution of BT nanoparticles was totally optically clear, 3 ml of PAH solution (10 mg ml^{-1} in 10 mM NaCl solution) was added, followed by 24 h of stirring (1500 rpm). Then, the barium titanate nanoparticles capsulated with PAH (BT@PAH) can be obtained after centrifugation under 8k rpm for 20 min. For the loading of RB, 2 ml of RB solution (2, 1, 0.5, 0.2 or 0.1 mg ml^{-1} in DMSO) was added to the BT-PAH solution, followed by 2 h of sonication and 24 h of stirring. The RB attached BT@PAH (BT@PAH/RB) nanoparticles can be obtained after centrifugation under 8k rpm for 20 min. BT@PAH/RB/PAH was synthesized using the same method illustrated

above, and the final product (recorded as BT–RB for simplicity) was dissolved in 30 ml DI water and kept in dark for further use.

2.5 *Ex vivo* ROS detection

$^1O_2$ is the most important kind of ROS in PDT, thus we evaluated the one-photon excited $^1O_2$ production of BT–RB (0.25 mg ml^{-1} in DI water), SHG-mediated $^1O_2$ production of RB (6.23 μg ml^{-1} in DI water), BT–RB (0.25 mg ml^{-1} in DI water) and mixed solution of BT nanoparticles (0.25 mg ml^{-1} in DI water) and RB (6.23 μg ml^{-1} in DI water) by using two kinds of $^1O_2$ indicator, ABDA[40] and DPBF.[41] For ABDA-related experiments, the solution to be tested was mixed with ABDA (1 mg ml^{-1} in DMSO), followed by the light irradiation. 532 nm laser light (30 mW) was used in one-photon excitation and 1040 nm fs laser light was used in SHG-mediated excitation. The absorption spectra were recorded every 3 min for one-photon excitation and every 10 min for SHG-mediated excitation, and the decrease of absorption values at 377 nm was used as the quantitative indicator of $^1O_2$ production.

For DPBF-related experiments, we mixed the test solution with DPBF (10 mM) and irradiated the mixture using 1040 nm fs laser. The absorption spectra were recorded every 5 min, and the decrease of absorption values of DPBF was used as the quantitative indicator of $^1O_2$.

2.6 Cell culture

Hela cells (human cervical cancer cell line, purchased from the Cell Culture Center of the Institute of Basic Medical Sciences, Chinese Academy of Medical Sciences) were used for all the *in vitro* experiments in this work. The cells were grown in DMEM media supplemented with 10% of FBS (contains penicillin and amphotericin B), and the incubation environment was kept at 37 °C and 5% of CO_2.

2.7 *In vitro* cell imaging

The Hela cells were first seeded in cultivation dishes (35 mm) with confluence of 50–60%. One day later, during the treatment, certain concentration of treat solution was added into the dishes. 2 hours later, the cells were all washed with PBS for 3 times to remove the incubation solution and then imaged using the scanning microscope.

The imaging system we built was illustrated in Fig. S2.† Briefly, the 1040 nm fs laser light was first guided into the microscope, passing through a scanning module and a 980 dichroic mirror and focused by an objective lens (20×, Olympus). After the excitation, the signal was collected by the same objective lens and finally detected by photomultiplier tubes (PMT) after passing specific dichroic mirrors and optical filters. PMT-1 was used to detect the signal with wavelength between 495 nm and 540 nm (recorded as green channel), while PMT-2 was used to detect the signal with wavelength between 570 nm and 625 nm (recorded as red channel).

During the imaging process, the excitation power was 100 mW, and the integration time of each pixel was set as 10 μs.

2.8 Intracellular ROS detection

DCFH-DA was used to evaluate the intracellular ROS generation ability.[42] Briefly, the drug treated Hela cells was fed with DCFH-DA and incubated for 30 min, followed by washing with PBS for 3 times. Afterwards, the cells were imaged using the imaging system we described above.

2.9 *In vitro* cytotoxicity of BT–RB

In this work, CCK-8 assay was used to evaluate the *in vitro* cytotoxicity of BT–RB.[43] Briefly, Hela cells were first seeded in a 96-well culture plate (5×10^3 per well) and cultivated for 24 h; then 100 μl of DMEM with different concentrations of BT–RB nanoparticles (0, 1, 2, 5, 10, 20, 50 μg ml^{-1}) was added in certain wells, followed by 24 h of cultivation. Afterwards, the medium was washed 3 times using PBS solution, and 10 μl of CCK-8 solution was added into each well. After keeping the plate in dark for another 4 h, the OD value at 450 nm was used as the indicator of the cell viability.

2.10 *In vitro* PDT of cells

After the incubation with certain treatment solution, the Hela cells were put into the imaging system illustrated above. The PDT process was applied just by scanning a fixed square region (located at the center of the imaging field and has the size of half of the area) for cycles. During PDT treatment, the excitation power under the objective lens was 100 mW, and the integration time at each pixel was set as 20 μs.

2.11 Evaluation of *in vitro* cell apoptosis

Annexin V and PI assays were used to evaluate the *in vitro* cell apoptosis. Briefly, the drug treated Hela cells were washed 3 times, and were incubated with 1 ml of incubation medium containing 10 μl of Annexin V (20 μg mL^{-1}) and 20 μl of PI (50 μg mL^{-1}) for another 5 min. Afterwards, the cells were washed for 3 times and imaged every 120 scan-cycles of PDT treatment to monitor the therapeutic effect.

3. Results and discussions

3.1 Characterization of BT nanoparticles and RB

The BT nanoparticles powder was first dissolved in DI water, and sonicated until the solution became optically clear before use. The TEM image of BT in Fig. 1(a) shows that the BT nanoparticles have the size around 70 nm. By using a home-built cage system, the SHG property of BT nanoparticles was verified under the irradiation of a 1040 nm fs laser. When the BT nanoparticles powder was focused by the 1040 nm fs laser, bright green light could be observed clearly. As shown in Fig. 1(b), the SHG signal we measured was located exactly at the 520 nm and had a narrow full width with half maxima (FWHM) of 3.06 nm. Afterwards, the optical property of RB in DMSO solution was also checked. From Fig. 1(c), we can see that the absorption peak of RB is at 548 nm (with a shoulder at 515 nm), and the fluorescence emission peak is at 572 nm under excitation of a 520 nm LED, which means that RB could absorb
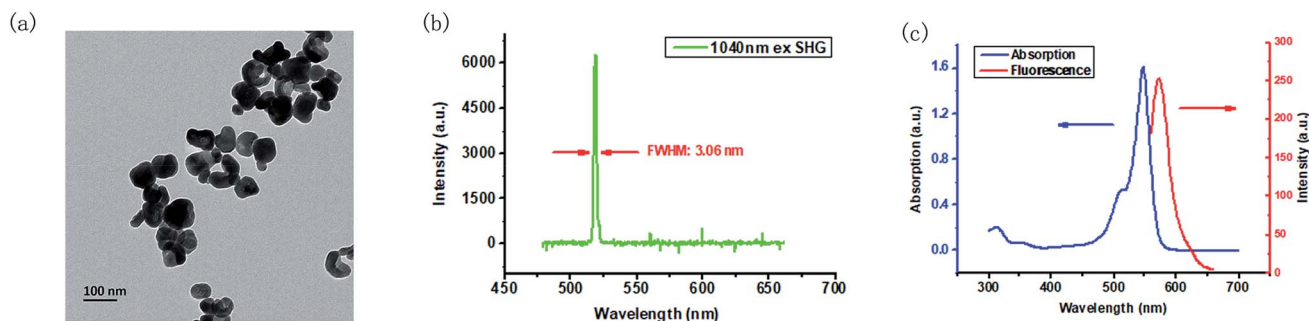
Fig. 1 Characterization of BT nanoparticles and RB molecules. (a) TEM image of BT nanoparticles; (b) SHG spectrum of BT excited by 1040 nm fs laser; (c) absorption spectrum (blue curve) and fluorescence spectrum (red curve) of RB molecules.

520 nm light efficiently, and could emit fluorescence between 550 nm and 650 nm.

3.2 Synthesis and characterization of BT–RB nanoparticles

The electrostatic absorption method was used to achieve effective combination of BT nanoparticles and RB molecules. Since BT nanoparticles and RB molecules are both negatively charged, positively charged PAH was used as the adhesive. Specifically, PAH, RB and PAH were absorbed in sequence on the nanoparticles, and the final product was called BT–RB for simplicity. UV spectra and zeta potentials were used to record the synthesis procedure. As shown in Fig. 2(a), BT has no absorption peak longer than 400 nm, while BT@PAH/RB

showed the same envelop between 500 nm to 600 nm as that of RB in Fig. 1(c). However, BT@PAH/RB is not stable in DI water (Fig. S3†). To solve this problem, an additional PAH layer was coated at the surface of the nanoparticle. Absorption of the final product, BT@PAH/RB/PAH (BT–RB), was shown as the blue curve in Fig. 2(a), and the photo of the BT–RB solution was also shown as the inset of Fig. 2(a). The pink solution and the envelop between 500 nm and 600 nm indicate the successful modification of RB. Moreover, the zeta potential was also measured during the procedure, and it changed between positive and negative in sequence (shown in Fig. 2(b)), which coincidence well with the synthesis procedure of BT–RB nanoparticles. Raman spectrum is a typical "finger print" for
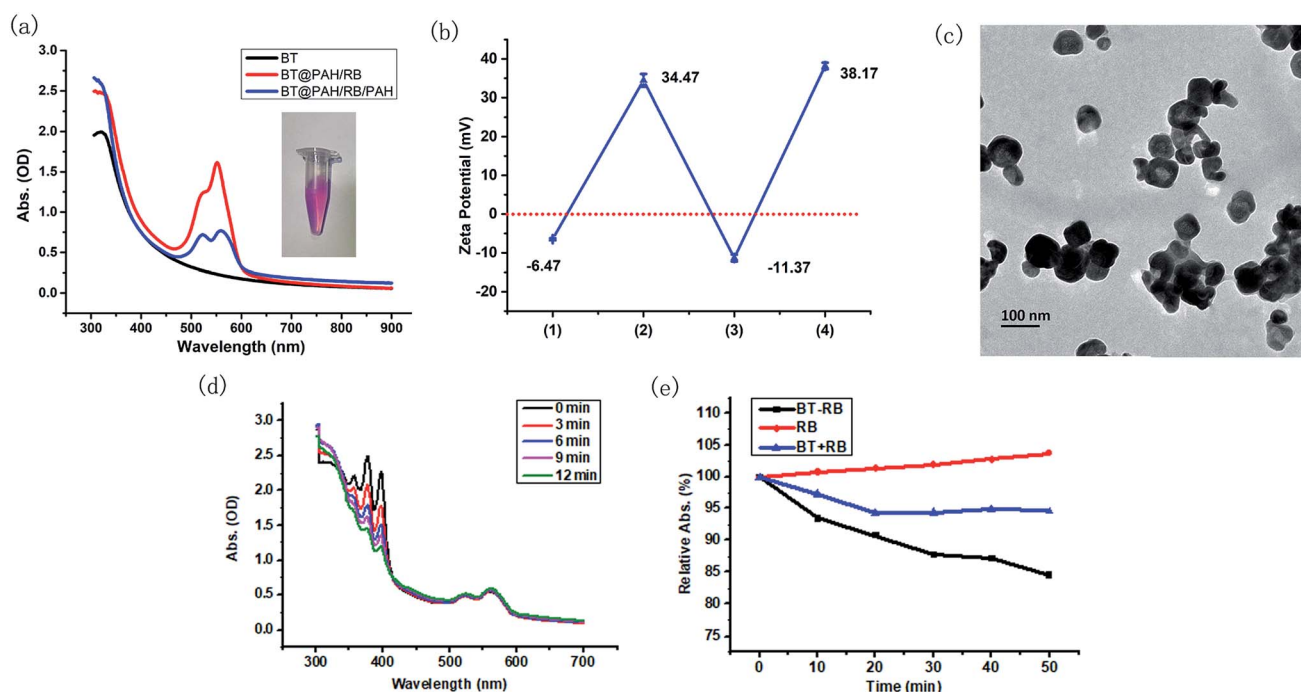

Fig. 2 Synthesis and characterization of BT−RB nanoparticles. (a) Absorption spectra of BT (black), BT@PAH/RB (red) and BT@PAH/RB/PAH (blue) (inset: photo of the final production); (b) changes in zeta potential of nanoparticles during the synthesis process, (1) is BT, (2) is BT@PAH, (3) is BT@PAH/RB, (4) is BT@PAH/RB/PAH (BT−RB); (c) TEM image of BT−RB; (d) absorption spectra of BT−RB and ABDA mixture irradiated by 532 nm laser for different time periods; (e) relative 377 nm-light absorption values of ABDA mixed with RB (red), BT + RB (blue) and BT−RB (black) as the irradiation time of 1040 nm fs laser increases. Error bars indicate SD.

molecules, and can be used for molecular detection.[44] By using a fiber-based Raman probe (BWTEK) under the excitation of 785 nm laser (300 mW), we have measured the Raman spectra of RB aqueous solution, BT powder, PAH particles and BT–RB. As can be seen from Fig. S4,† peaks of RB at 612 cm^{-1} (ν(C–I)), 1259 cm^{-1} (δ(CCC) ring + δ(C–H)), 1288 cm^{-1} (δ(CCC) ring + δ(C–H)), 1495 cm^{-1} (ν_{as}(C=C) ring) and 1612 cm^{-1} (ν_s(C=C) ring)[45] does not appear in BT and PAH, but coincidence well with those in BT–RB. At the same time, we could also find that the ratio between the intensities of 308 cm^{-1} and 612 cm^{-1} in BT–RB (0.606) is about the twice of that in RB (0.303). We attribute this to the existence of BT, who also has a strong peak at 308 cm^{-1}. Since the peaks of RB and BT are both appear in the Raman spectrum of BT–RB, we could confirm the successful loading of RB on BT. By comparing the absorption curve with that of RB molecule and BT nanoparticles, the final concentration of RB loaded on BT nanoparticles was calculated and showed in Table S1.† Though the loading amount is the most when concentration of added RB is 2 mg ml^{-1}, it shows no much difference but means much lower loading efficiency when comparing with that of 1 mg ml^{-1}. Therefore we used the 1 mg ml^{-1} as the added RB concentration to make BT–RB for further use, and the corresponding concentration of loaded RB is 6.23 μg ml^{-1} (with BT nanoparticles concentration of 0.25 mg ml^{-1}).

The morphology of BT–RB nanoparticles was checked by TEM images. As shown in Fig. 2(c), the shape of BT–RB nanoparticles was almost the same as that of BT nanoparticles except for the thin film on the surface, which was due to the modification of PAH and RB. $^1O_2$ is the most important kind of ROS in PDT, to verify the ROS production ability of BT–RB under one photon excitation, we used a 532 nm laser (30 mW) as the excitation source and a common $^1O_2$ indicator, ABDA. As shown in Fig. 2(d), the absorption value of ABDA dropped sharply and almost disappeared in 12 min, while the part of spectrum corresponding to BT–RB remains the same. This showed the good $^1O_2$ production ability of BT–RB, and indicated the probability for SHG-mediated $^1O_2$ production. To study the SHG-mediated $^1O_2$ production ability of BT–RB nanoparticles, a 1040 nm fs laser was used as the excitation source and three different solutions were used for comparison: RB solution; mixed solution of BT nanoparticles and RB (recorded as BT + RB); BT–RB nanoparticles solution. From Fig. 2(d), it could be found that under 1040 nm fs laser irradiation, RB has negligible $^1O_2$ production, BT + RB has weak ability to generate $^1O_2$, while BT–RB showed the greatest ability to generate $^1O_2$. At the same time, the SHG mediated $^1O_2$ generation abilities of RB, BT + RB and BT–RB were also evaluated using another common $^1O_2$ indicator, DPBF. As shown in Fig. S5,† under the excitation of 1040 nm laser, RB generated little $^1O_2$, BT + RB could generate more, and BT–RB generated the most. These results indicated that: first, the two-photon excited photodynamic effect is very weak for RB molecules; second, the free BT nanoparticles around RB molecules could enhance the photodynamic effect of RB to some extend; third, the BT–RB nanocomposites perform better than a simple mixture of BT nanoparticles and RB. However, more information of energy transfer process is needed for detailed explanations.

3.3 *In vitro* cell imaging

In vitro cell imaging was used to study the cell uptake of the nanoparticles and the energy transfer process. A common used cell line, Hela cells, was used in all the *in vitro* experiment. The cells were divided into 4 groups, and respectively treated with: BT nanoparticles solution; RB solution; BT + RB solution; BT–RB nanoparticles solution. After 2 h of incubation and washing carefully for 3 times, the cells were imaged under a home-built imaging system (shown in Fig. S2†). During the imaging process, the SHG signal of BT nanoparticles has the wavelength of 520 nm, which could be detected by PMT-1, while the fluorescence signal (one/two-photon excited) of RB is mainly between 550 nm to 600 nm and could be detected by PMT-2. Both speculations were confirmed by the first two columns of Fig. 3. The SHG signal seemed grainier, while the fluorescence signal seemed finer and uniform. In the case of BT + RB, we could see both SHG signals and fluorescence signals, but their positions did not coincidence well, which confirmed the free state of BT nanoparticles and RB molecules. When comparing the first and the third columns, we could find that the SHG signal of BT + RB is a little weaker than that of BT nanoparticles. When comparing the second and the third columns, we could find that the fluorescence of BT + RB is a bit stronger than that of RB solution. In the case of BT–RB nanoparticles, we could also observe both SHG signals and fluorescence signals, but the SHG signals were weaker and the fluorescence signals were stronger. All the observed intensity comparison was visualized and confirmed in Fig. S6† as statistics of the average intensity per pixel in both red channel and green channel of each image. At the same time, despite the SHG signals of BT–RB are weaker than the fluorescence signals, which means less points for analysis, we still calculated the Pearson's correlation coefficient of the merge image of BT + RB and BT–RB. The Pearson's correlation coefficient of BT–RB (0.3614) is obviously higher than that of BT + RB (0.1228), indicating the better co-localization of BT and RB in BT–RB. From the above analysis, we could conclude that in the case of BT + RB and BT–RB, the signals were not simply mixed when the RB molecules were combined with BT nanoparticles. Furthermore, since the SHG signals became weaker and the fluorescence signals became stronger when BT nanoparticles and RB were combined more closely, we concluded that: when BT nanoparticles were absent, the fluorescence signals of RB were all produced by the direct excitation of 1040 nm fs laser, otherwise the SHG signal produced by BT nanoparticles can be absorbed by RB and acted as an addition one-photon fluorescence excitation source. Once the photosensitizer was excited to the excitation energy level, the transition would bring it to the photodynamic process, which made it possible for ROS production.

3.4 Intracellular ROS detection

A commonly used intracellular indicator, DCFH-DA, was used to evaluate the ROS production ability of BT–RB inside the cells. When DCFH-DA was taken up by the cells, it would be transferred into DCFH. The DCFH could be oxidized to DCF, which can emit green light under excitation. Similar to *in vitro*
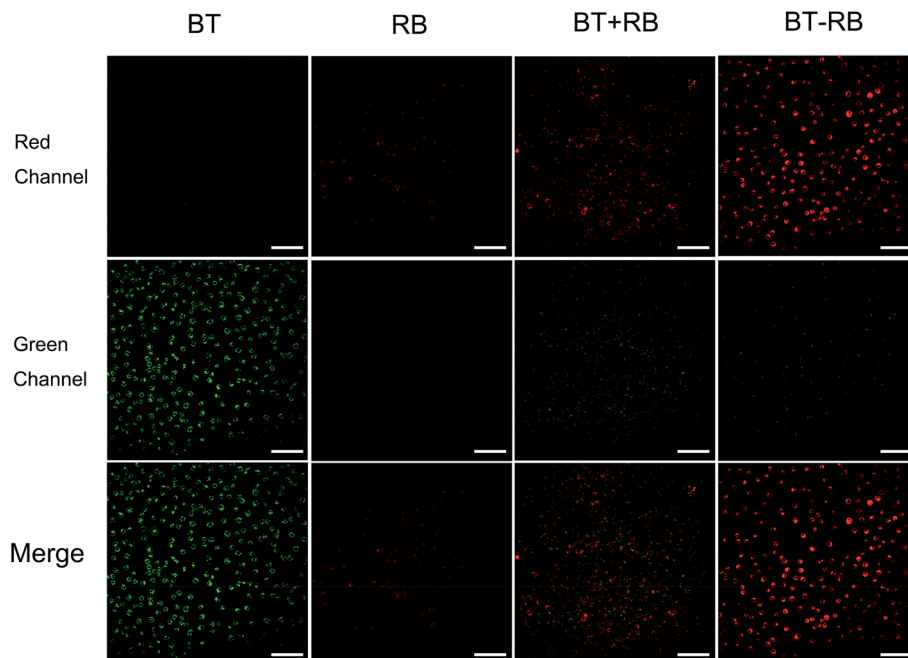
Fig. 3 *In vitro* microscopy imaging of Hela cells after different treatments. Scale bar: 100 μm.

imaging, the cells are also divided to 4 groups. Before imaging, all the cells were incubated with DCFH-DA for 30 min. During the imaging process, the green light produced by DCF (two-photon excited) could be detected by PMT-1. To distinguish SHG signal from the fluorescence of DCF, the fluorescence can be recognized as molecular signals of smaller spot size, which exist everywhere in the cell outline. Fig. 4(a)–(d) show the imaging results in green channels. We calculated the average

intensity per pixel in each image and draw the statistic results as Fig. 4(e). By combining images in Fig. 4(a)–(d), results in Fig. 4(e) and the data of green channels in Fig. S6,† we could find that though BT has no ability to produce ROS, it could play a helpful role in the ROS production of RB, especially when BT and RB were combined closer. When we combined this phenomenon with the previous conclusions for *in vitro* imaging, we could make the following conclusions: (1) the fluorescence
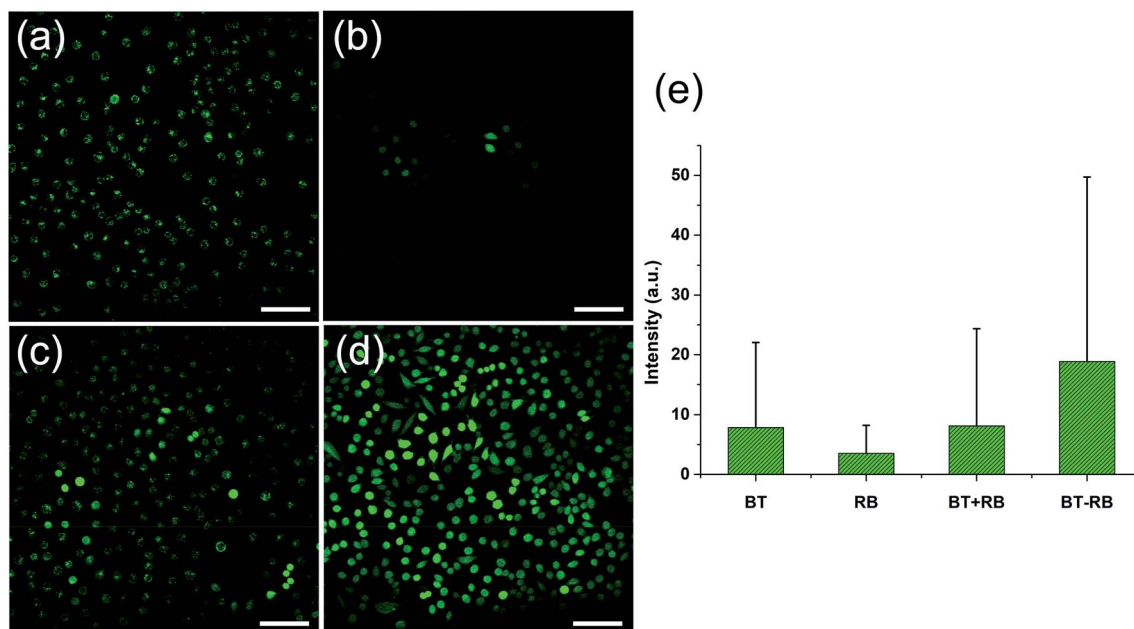

Fig. 4 1040 nm fs laser excited imaging of (a) BT, (b) RB, (c) BT + RB and (d) BT−RB using green channel after incubated with DCFH-DA. (e) The statistics of the average signal intensity per pixel in each image. Scale bar: 100 μm. Error bars indicate SD.

emission and ROS production of RB excited by 1040 nm fs light were rather weak; (2) the SHG from BT accounted for the enhancement of both fluorescence and ROS production of RB; (3) the BT–RB composite nanoparticles performed the best among the four groups. These conclusions can guide us for further SHG enhanced PDT experiments.

3.5 *In vitro* cytotoxicity of BT–RB

Before *in vitro* PDT, CCK-8 assay was used to evaluate the cytotoxicity of BT–RB nanoparticles. Briefly, cells treated with different concentrations were incubated for 24 h before adding CCK-8 solution and sent for cell viability analysis. As shown in Fig. S7,† the cell viability shows no significant decline with the increase of concentration, which indicates the negligible cytotoxicity of BT–RB.

3.6 1040 nm fs laser excited PDT *in vitro*

In vitro PDT was applied by repeatedly scanning a fixed region, which was defined as the region located at the centre with the size of half of the total view area. During the process, Annexin V and PI assays were used to evaluate the therapeutic effect. Annexin V is sensitive to the early stage of cell apoptotic, while PI is sensitive to the late stage of cell apoptotic and cell necrosis. Thus the combination of Annexin V and PI could indicate the cell state.[46,47]

In our work, we recorded the cell state by taking an image every 120 scan-cycles. During the imaging process, Annexin V could emit fluorescence around 525 nm and PI could emit fluorescence around 615 (both belonged to two-photon excitation), which could be detected by PMT-1 and PMT-2, respectively. To distinguish the fluorescence of Annexin V/PI from the signals of the treatment reagent, all the results were compared with the images token at the very beginning before PDT.

Fig. 5 shows the results of PDT on BT–RB nanoparticles treated cells. It could be found that the fluorescence intensity of RB in scanning area (squared out by white dashed line) decreased along with the treatment, which is due to the bleaching of fluorescence. Starting from the 240th scan-cycle, strong signals appeared in the scanned area, where the red and green channels coincide well and gave the yellow pseudo color in the merged images. The signals outlined the shapes of death cells, thus could be recognized as the fluorescence of Annexin V/PI. As a sign for cell death, the fluorescence of Annexin V/PI increased as the treatment goes on, which means that new death cells emerge constantly. Then we used the Image J® software to analyse the colocalization of the signals in red and green channel of the white line squared area in 480th scans image. The scatter plot was shown in Fig. S8,† from which we could find that the intensities of Annexin V and PI are comparably high. Then, the Pearson's correlation coefficient was also calculated as 0.953, which means that the signals in red and green channel coincidence well and the fluorescence of Annexin V and PI came from same points. The above analysis has confirmed the PDT induced cell apoptosis by BT–RB. Furthermore, the fluorescence of Annexin V/PI could only be observed in the scanned area, which confirmed the good selectivity and localized therapy ability of SHG enhanced PDT.

For comparison, Fig. S9† shows the results of PDT on BT + RB nanoparticles treated cells. As the treatment went on, the bleaching of RB fluorescence could also be observed, but the signal of Annexin V/PI did not appear this time, which means that the ROS produced by BT + RB is not enough to cause significant cell death.

For the control groups, BT–RB treated cells and BT + RB treated cells were scanned for 480 cycles without the treatment of Annexin V/PI. As shown in Fig. S10† (the first two columns belong to BT–RB, the last two columns belong to BT + RB), no
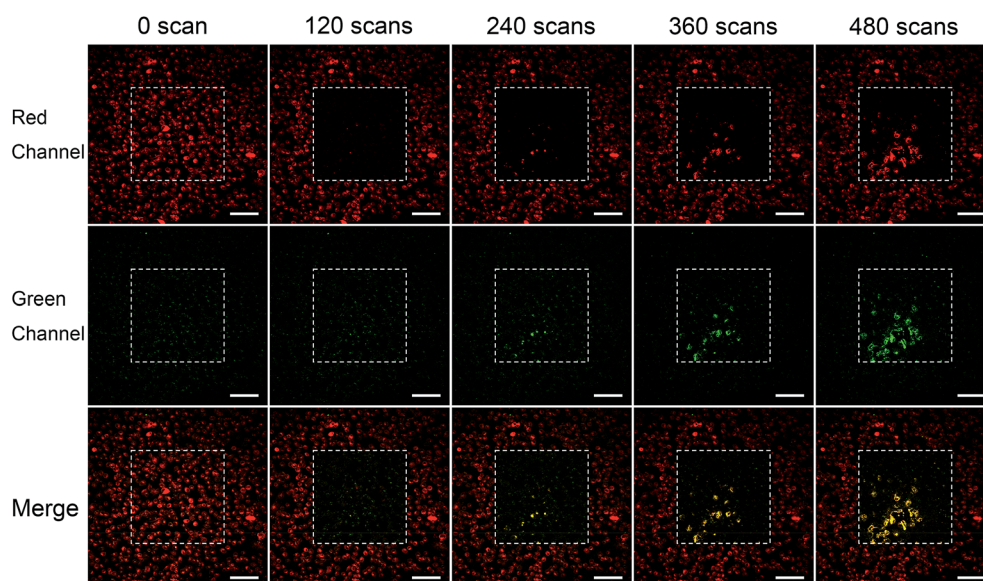

Fig. 5 Evaluation of localized PDT after treated with BT–RB nanoparticles under 1040 nm fs laser irradiation. The white dashed lines square out the scanning areas. Scale bar: 100 μm.

sign for cell death could be observed, which confirmed that the strong signals in the scanned area in BT–RB case were due to the fluorescence of Annexin V/PI.

These phenomena indicated that BT–RB has the good ability for localized NIR light excited PDT treatment in cell level, and performed better than BT + RB.

4. Conclusions

By using the electrostatic absorption method, we have introduced in the present paper novel BT–RB nanoparticles with the ability to achieve SHG enhanced photodynamic effect. The subsequent *in vitro* experiments have shown that BT–RB nanoparticles have the ability to produce ROS in Hela cells and can cause cell death in a defined fixed area under the excitation of 1040 nm fs laser. It is also proved that the close combination of BT and RB can bring improvement on the total ROS production. When BT–RB is irradiated by the NIR light (1040 nm), the RB is excited by two-photon absorption and emit fluorescence and produce ROS. Simultaneously, the NIR light was convert to green light (520 nm) by BT, which can act as an additional one-photon excitation source for RB. As BT can be excited by neither 1040 nm light nor 520 nm light, it just act as a light converter in the whole system. At the same time, in a non-linear or linear way, RB can be excited and generate all the ROS, act as the functional part of the whole system. When BT and RB get closer, the one-photon excitation efficiency can be higher, resulting in more ROS production. Furthermore, a comparison of PDT therapeutic effect between BT–RB and the mixed solution of BT and RB has also been studied, from which we can draw the conclusion that BT–RB nanoparticles have a better performance and the composite nanoparticles of harmonic crystals and PSs are rather promising in localized NIR light excited PDT treatment.

Conflicts of interest

There are no conflicts to declare.

Acknowledgements

References

1 F. Bray, J. Ferlay, I. Soerjomataram, R. L. Siegel, L. A. Torre and A. Jemal, *Ca-Cancer J. Clin.*, 2018, **68**, 394–424.

2 T. Ten Bruggencate, K. G. Luijkx and J. Sturm, *Ageing Soc.*, 2018, **38**, 1745–1770.

3 D. Li, N. A. de Glas and A. Hurria, *Clin. Geriatr. Med.*, 2016, **32**, 1–15.

4 M. Serrano, *Carcinogenesis*, 2016, **37**, 107.

5 M. B. Vrouenraets, G. W. M. Visser, G. B. Snow and G. A. M. S. van Dongen, *Anticancer Res.*, 2003, **23**, 505–522.

6 H. A. Collins, M. Khurana, E. H. Moriyama, A. Mariampillai, E. Dahlstedt, M. Balaz, M. K. Kuimova, M. Drobizhev, V. X. D. Yang, D. Phillips, A. Rebane, B. C. Wilson and H. L. Anderson, *Nat. Photonics*, 2008, **2**, 420–424.

7 J. Qian, A. Gharibi and S. L. He, *J. Biomed. Opt.*, 2009, **14**, 014012.

8 X. H. Sun, A. Zebibula, X. B. Dong, G. H. Li, G. X. Zhang, D. Q. Zhang, J. Qian and S. L. He, *Nano Res.*, 2018, **11**, 2756–2770.

9 T. J. Dougherty, C. J. Gomer, B. W. Henderson, G. Jori, D. Kessel, M. Korbelik, J. Moan and Q. Peng, *J. Natl. Cancer Inst.*, 1998, **90**, 889–905.

10 B. W. Henderson and T. J. Dougherty, *Photochem. Photobiol.*, 1992, **55**, 145–157.

11 I. J. Macdonald and T. J. Dougherty, *J. Porphyrins Phthalocyanines*, 2001, **05**, 105–129.

12 K. Haedicke, S. Graefe, U. Teichgraeber and I. Hilger, *Biomed. Opt. Express*, 2016, **7**, 2641–2649.

13 X. Huang and M. A. El-Sayed, *J. Adv. Res.*, 2010, **1**, 13–28.

14 L. Yuan, W. Y. Lin, K. B. Zheng, L. W. He and W. M. Huang, *Chem. Soc. Rev.*, 2013, **42**, 622–661.

15 Y. L. Wang, R. R. Hu, W. Xi, F. H. Cai, S. W. Wang, Z. F. Zhu, R. P. Bai and J. Qian, *Biomed. Opt. Express*, 2015, **6**, 3783–3794.

16 S. S. Lucky, K. C. Soo and Y. Zhang, *Chem. Rev.*, 2015, **115**, 1990–2042.

17 A. B. Ormond and H. S. Freeman, *Materials*, 2013, **6**, 817–840.

18 M. C. DeRosa and R. J. Crutchley, *Coord. Chem. Rev.*, 2002, **233**, 351–371.

19 S. J. Im, S. Y. Lee and Y. I. Park, *Appl. Chem. Eng.*, 2018, **29**, 138–146.

20 M. Pawlicki, H. A. Collins, R. G. Denning and H. L. Anderson, *Angew. Chem., Int. Ed.*, 2009, **48**, 3244–3266.

21 L. K. McKenzie, I. V. Sazanovich, E. Baggaley, M. Bonneau, V. Guerchais, J. A. G. Williams, J. A. Weinstein and H. E. Bryant, *Chem.–Eur. J.*, 2017, **23**, 234–238.

22 F. Helmchen and W. Denk, *Nat. Methods*, 2005, **2**, 932–940.

23 J. Qian, D. Wang, F. H. Cai, Q. Q. Zhan, Y. L. Wang and S. L. He, *Biomaterials*, 2012, **33**, 4851–4860.

24 D. Y. Li, H. Q. Zhang, L. L. Chu, X. Y. Zhao and J. Qian, *Opt. Quantum Electron.*, 2015, **47**, 3081–3090.

25 Q. Zou, H. Zhao, Y. Zhao, Y. Fang, D. Chen, J. Ren, X. Wang, Y. Wang, Y. Gu and F. Wu, *J. Med. Chem.*, 2015, **58**, 7949–7958.

26 N. T. Chen, K. C. Tang, M. F. Chung, S. H. Cheng, C. M. Huang, C. H. Chu, P. T. Chou, J. S. Souris, C. T. Chen, C. Y. Mou and L. W. Lo, *Theranostics*, 2014, **4**, 798–807.

27 Y. Shen, A. J. Shuhendler, D. Ye, J. J. Xu and H. Y. Chen, *Chem. Soc. Rev.*, 2016, **45**, 6725–6741.

28 N. Alifu, X. B. Dong, D. Y. Li, X. H. Sun, A. Zebibula, D. Q. Zhang, G. X. Zhang and J. Qian, *Mater. Chem. Front.*, 2017, **1**, 1746–1753.

29 B. Gu, W. B. Wu, G. X. Xu, G. X. Feng, F. Yin, P. H. J. Chong, J. L. Qu, K. T. Yong and B. Liu, *Adv. Mater.*, 2017, **29**, 1701076.

30 P. A. Franken, G. Weinreich, C. W. Peters and A. E. Hill, *Phys. Rev. Lett.*, 1961, **7**, 118–119.

31 A. V. Kachynski, A. N. Kuzmin, M. Nyk, I. Roy and P. N. Prasad, *J. Phys. Chem. C*, 2008, **112**, 10721–10724.

32 A. V. Kachynski, A. Pliss, A. N. Kuzmin, T. Y. Ohulchanskyy, A. Baev, J. Qu and P. N. Prasad, *Nat. Photonics*, 2014, **8**, 455–461.

33 B. B. Gu, A. Pliss, A. N. Kuzmin, A. Baev, T. Y. Ohulchanskyy, J. A. Damasco, K. T. Yong, S. C. Wen and P. N. Prasad, *Biomaterials*, 2016, **104**, 78–86.

34 X. Y. Zhou, Y. Chen, J. Su, X. H. Tian, Y. H. Luo and L. Luo, *RSC Adv.*, 2017, **7**, 52125–52132.

35 G. G. Genchi, A. Marino, A. Rocca, V. Mattoli and G. Ciofani, *Nanotechnology*, 2016, **27**, 232001.

36 D. Staedler, T. Magouroux, R. Hadji, C. Joulaud, J. Extermann, S. Schwungi, S. Passemard, C. Kasparian, G. Clarke, M. Gerrmann, R. Le Dantec, Y. Mugnier, D. Rytz, D. Ciepielewski, C. Galez, S. Gerber-Lemaire, L. Juillerat-Jenneret, L. Bonacina and J. P. Wolf, *ACS Nano*, 2012, **6**, 2542–2549.

37 P. Pantazis, J. Maloney, D. Wu and S. E. Fraser, *Proc. Natl. Acad. Sci. U. S. A.*, 2010, **107**, 14535–14540.

38 S. W. Wang, X. Y. Zhao, J. Qian and S. L. He, *RSC Adv.*, 2016, **6**, 40615–40625.

39 J. Paczkowski, J. J. Lamberts, B. Paczkowska and D. C. Neckers, *J. Free Radicals Biol. Med.*, 1985, **1**, 341–351.

40 O. Planas, N. Macia, M. Agut, S. Nonell and B. Heyne, *J. Am. Chem. Soc.*, 2016, **138**, 2762–2768.

41 R. Venkatesan, N. Periasamy and T. S. Srivastava, *Proc. Indiana Acad. Sci.*, 1992, **104**, 713–722.

42 A. R. Rosenkranz, S. Schmaldienst, K. M. Stuhlmeier, W. J. Chen, W. Knapp and G. J. Zlabinger, *J. Immunol. Methods*, 1992, **156**, 39–45.

43 H. Tominaga, M. Ishiyama, F. Ohseto, K. Sasamoto, T. Hamamoto, K. Suzuki and M. Watanabe, *Anal. Commun.*, 1999, **36**, 47–50.

44 A. Rygula, K. Majzner, K. M. Marzec, A. Kaczor, M. Pilarczyk and M. Baranska, *J. Raman Spectrosc.*, 2013, **44**, 1061–1076.

45 A. M. Gabudean, M. Focsan and S. Astilean, *J. Phys. Chem. C*, 2012, **116**, 12240–12249.

46 H. Sawai and N. Domae, *Biochem. Biophys. Res. Commun.*, 2011, **411**, 569–573.

47 S. Chen, A. C. Cheng, M. S. Wang and X. Peng, *World J. Gastroenterol.*, 2008, **14**, 2174–2178.